Biomaterials 35 (2014) 6106–6117

Contents lists available at ScienceDirect

Biomaterials

journal homepage: www.elsevier.com/locate/biomaterials

Targeting efficiency of RGD-modified nanocarriers with different ligand intervals in response to integrin αvβ3 clustering

Zhaoming Guo, Bing He, Hongwei Jin, Haoran Zhang, Wenbing Dai, Liangren Zhang, Hua Zhang, Xueqing Wang, Jiancheng Wang, Xuan Zhang, Qiang Zhang*

State Key Laboratory of Natural and Biomimetic Drugs, School of Pharmaceutical Sciences, Peking University, Beijing 100191, China

ARTICLE INFO

Article history:
Received 11 February 2014
Accepted 10 April 2014
Available online 1 May 2014

Keywords:
Liposomes
Integrin αvβ3 clustering
RGD
Targeted delivery
Anticancer

ABSTRACT

Receptor change induced by ligand binding is a new issue to face in the field of targeted delivery. Receptor clustering, the main pattern of receptor changes, decreases the affinity between ligand and receptor due to the redistribution of receptor position. In an attempt to respond to such challenge, we designed and constructed three RGD-modified nanocarriers with different ligand intervals: stealth liposomes modified with the monomeric RGD (moRGD-LP), dimeric RGD (diRGD-LP) and a special dimeric RGD with a linker between two cyclic RGD motifs (P-diRGD-LP). The αvβ3-positive and -negative tumor cells (Melanoma B16 and MCF-7) were used as the cell models. As a result, P-diRGD-LP demonstrated strongest interaction with B16 cells in surface plasmon resonance study and highest cellular uptake in B16 cells in real-time confocal analysis. The enhanced endocytosis of P-diRGD-LP was found to be αvβ3-mediated and P-diRGD-LP increased the involvement of the clathrin-dependent pathway. Importantly, P-diRGD-LP demonstrated the best targeting effect in B16-tumor bearing mice in both *in vivo* and *ex vivo* near-infrared fluorescent images, about 2.4-fold that of moRGD-LP and 2.8-fold that of diRGD-LP at 3 h. Further, we validated integrin αvβ3 clustering on B16 cells via a single-molecule imaging by a total internal reflection fluorescence microscopy. Finally, the 3D models of αvβ3 clustering suggested a receptor interval within 41.916–65.779 Å, while the molecular computation revealed an RGD ligand interval of 20.944 Å, 42.753 Å and 78.196 Å for diRGD-LP, P-diRGD-LP and moRGD-LP, respectively, confirming the best matching between clustered αvβ3 and P-diRGD-LP. In conclusion, P-diRGD-LP could achieve higher targeting to αvβ3-positive tumor via the enhanced interaction based on the better ligand-receptor compatibility. The design of targeted nanocarriers against receptor clustering might provide new insight into the nanotechnology-based anticancer therapy.

1. Introduction

Targeted drug delivery has attracted much attention in anticancer research because of the advantages of enhanced distribution in tumor sites and reduced side effects to normal tissues. Active targeting strategies rely on the biomarkers that are specifically overexpressed on tumor cells. These biomarker molecules function as specific receptors in plasma membrane for recognizing and binding extracellular specific ligands. Ligand binding activates the matched receptor, subsequently inducing the cellular uptake of nanomedicines via endocytosis pathway [1,2]. However, the ligand–receptor interplay also triggers the receptor change, including conformation change or redistribution in cell membrane [3,4]. During the last decades, ligand-modified nanocarriers have been extensively studied in searching for more specific targeting strategy for their potential clinical use in cancer therapy [5,6]. But little is concerned about the effect of receptor change induced by ligand binding on targeting efficacy of nanocarriers.

Receptor clustering, as a common response to ligand binding, happens in multiple kinds of receptors such as epidermal growth factor receptor (EGFR) and integrins [7,8]. Due to the assembly of activated receptors in cell membrane, the interval between receptors significantly decreases [9,10]. Obviously, this receptor clustering may affect its interaction with the ligands on the surface of nanocarriers, in the case of that the interval between ligands keeps unchanged. Indeed, the phenomenon of receptor clustering is reported to decrease the apparent affinity of the ligand for the receptor [11]. Currently, only few reports focus on receptor

* Corresponding author. Tel./fax: +86 10 82802791.
E-mail address: zqdodo@bjmu.edu.cn (Q. Zhang).

http://dx.doi.org/10.1016/j.biomaterials.2014.04.031
0142-9612/

clustering, although a great number of ligands have been designed and studied for targeted drug delivery. Therefore, it is necessary to establish a targeting strategy in response to receptor clustering for the improvement of targeted drug delivery.

αvβ3, one member of integrins, is an excellent target for tumor imaging and therapeutic application because of its high expression on tumor vasculature and tumor cells such as lung cancers, melanomas and brain tumors [12–15]. Crystal structures of the extracellular αvβ3 segment with and without ligand have provided insights into ligand binding and specificity [16,17]. As αvβ3 can recognize the Arg–Gly–Asp (RGD) sequence [18], a series of peptides containing the RGD sequence are developed for diagnosis and therapy of tumor [19–23]. In recent years, multivalent ligands, such as bivalency, seems promising to enhance the targeting efficacy of RGD peptides [24,25]. RGD dimers with different linkers exhibit distinct affinity with αvβ3 in tumor imaging studies [26]. The addition of PEG4 or Gly3 linker between two cyclic RGD motifs is particularly useful for improving tumor uptake in biodistribution and imaging studies. The integrin αvβ3 binding affinity of RGD dimer with PEG4 or Gly3 linker is better than that of regular RGD dimer with only one Glu linker. However, little attempt is made to develop a multivalent RGD-modified nanocarrier for tumor-targeted drug delivery. More importantly, the detailed mechanism of increased targeting efficacy is still unclear.

Based on the background above, we designed and constructed three RGD-modified nanocarriers with different ligand intervals, namely, stealth liposomes (LP) modified with the monomeric RGD (moRGD-LP), dimeric RGD (diRGD-LP) and a special dimeric RGD with a linker between two cyclic RGD motifs (P-diRGD-LP). The αvβ3-positive and -negative tumor cells (Melanoma B16 and MCF-7 cells) were used as the cell models. We investigated the interaction of these RGD-modified systems with B16 cells by surface plasmon resonance technique and the cellular uptake in B16 cells by real-time confocal analysis. The involvement of αvβ3 mediation and endocytosis pathway of these systems were studied. Their targeting efficacy in B16-tumor bearing mice was compared in both *in vivo* and *ex vivo* near-infrared fluorescent images. Finally, the calculation of receptor distance based on 3D models of αvβ3 clustering and the computation of RGD ligand intervals for each delivery system were conducted to confirm the best matching between clustered αvβ3 and RGD conjugated liposomes.

2. Materials and methods

2.1. Materials

DSPE–PEG_{2000} and NHS–PEG_{2000}–DSPE were obtained from the NOF Corporation (Tokyo, Japan) and egg phosphatidylcholine (EPC) was obtained from Lipoid GmbH (Ludwigshafen, Germany). Cholesterol (Chol), sucrose, methyl-beta-cyclodextrin (MβCD), and nystatin were purchased from Sigma–Aldrich (St. Louis, MO, USA). The fluorescent probe DiR was purchased from Biotium Inc. (Hayward, CA, USA). Hoechst 33258 and coumarin-6 was from Molecular Probes Inc. (Eugene, OR, USA). Cell counting kit-8 (CCK-8) was purchased from Dojindo Laboratories (Tokyo, Japan). BCA Protein Assay Kit was obtained from Applygen Technologies Inc. (Beijing, China). Sephadex G-50 was purchased from Pharmacia Biotech (Piscataway, NJ, USA). Cy3 mono NHS ester was purchased from GE Healthcare. CM5 sensor chips were purchased from GE Healthcare Bio-Sciences AB (Uppsala, Sweden). The monomeric c(RGDfK) peptide (moRGD or cRGD) was synthesized by ChinaPeptides Co., Ltd (Shanghai, China). E[c(RGDfK)]$_2$ (diRGD) and NH_2–PEG_4–Glu-[PEG_4-c(RGDfK)]$_2$ (P-diRGD) were synthesized by GL Biochem Peptide Ltd. (Shanghai, China).

B16 mouse melanoma cell line and MCF-7 human breast cancer cell line were purchased from the Institute of Basic Medical Science, Chinese Academy of Medical Science (Beijing, China). Cells were cultured in RPMI-1640 (Macgene Biotech Co., Ltd, Beijing, China) with 10% fetal bovine serum (FBS) and antibiotics (100 U/mL penicillin and 100 μg/mL streptomycin) at 37 °C in 5% CO_2.

Male 18–20 g C57BL/6 mice were purchased from Peking University Health Science Center. All mouse studies adhered to the principles of care and use of laboratory animals and were approved by the Institutional Animal Care and Use Committee of Peking University.

2.2. Preparation of different RGD peptides modified liposomes

Monomeric c(RGDfK) (moRGD or cRGD), common dimeric E[c(RGDfK)]$_2$ (diRGD) and flexible dimeric NH_2–PEG_4–Glu–[PEG_4–c(RGDfK)]$_2$ (P-diRGD) peptides were used here. P-diRGD was conjugated with DSPE–PEG_{2000}–NHS by the nucleophilic substitution reaction [27]. DSPE–PEG_{2000}–NHS was added to the solution of P-diRGD in fresh distilled DMF at 2:1 M ratio and the pH of the solution was adjusted to about 8.0 with triethylamine. The reaction was maintained for 5 days at room temperature under moderate stirring and traced by TLC. The reaction mixture was then put into a dialysis bag (MW cutoff = 3500 Da) against deionized water for 48 h at room temperature to remove the unconjugated peptide and reaction medium. The final solution was lyophilized. The methods of conjugation of moRGD and diRGD to DSPE–PEG_{2000}–NHS were the same as the method above. The conjugation efficiency was monitored by the high performance liquid chromatography (HPLC) system (Shimadzu, Japan). All the conjugation products were confirmed by MALDI–TOF MS.

To compare the targeting efficacy of the three types of RGD peptides modified liposomes, moRGD-LP, diRGD-LP, and P-diRGD-LP were prepared. No RGD peptide modified liposomes (LP) were also prepared as control. P-diRGD-LP was composed of EPC/Chol/DSPE–PEG_{2000}/P-diRGD–PEG–DSPE (65:20:3.93:0.45, mol/mol). To ensure that the total individual cyclic RGD number on the surface of the targeted liposomes were the same, moRGD-LP was composed of EPC/Chol/DSPE–PEG_{2000}/moRGD–PEG–DSPE (65:20:3.48:0.9, mol/mol) and diRGD-LP was composed of EPC/Chol/DSPE–PEG_{2000}/diRGD–PEG–DSPE (65:20:3.93:0.45, mol/mol). All coumarin-6-loaded liposomes (lipids: coumarin-6 = 1000:1, w/w) were prepared using the lipid film hydration method as described previously [28]. Briefly, the lipids and coumarin-6 were co-dissolved in chloroform/methanol (2:1, v/v) mixture and evaporated at 37 °C under reduced pressure. Then the thin film was hydrated with phosphate buffered saline (PBS, pH7.4), followed by sonication at 37 °C for 20 min. The liposomal suspension was eluted by a Sephadex G-50 column to remove unencapsulated coumarin-6.

For *in vivo* imaging studies, the DiR (lipids: DiR = 1000:5, w/w) as near-infrared fluorescent probe was loaded into liposomes with the same method as coumarin-6-loaded liposomes prepared.

2.3. Characterization of different RGD peptides modified liposomes

The particle size and zeta potential of the nanocarriers were measured by dynamic light scattering (DLS) using a Malvern Zetasizer (Nano ZS, Malvern, UK) at 25 °C. The morphology of liposomes was evaluated by cryogenic transmission electron microscopy (cryo-TEM). Samples were prepared by applying approximately 7 μL of the aqueous solution containing liposomes (40 μg/mL in distilled water) to a carbon grid and the excess liquid was removed by a filter paper. The frozen grids were stored in liquid nitrogen and transferred in a cyro-transfer holder (Gatan, Inc., Warrendale, Pennsylvania, USA) under liquid nitrogen at approximately −190 °C. Images were acquired with a Gatan US4000 UHS CCD camera (Gatan, Inc., Warrendale, Pennsylvania, USA). The encapsulation efficiency (EE) of coumarin-6/DiR was determined using a fluorescence spectroscope (Cary Eclipse, Varian Corporation, USA) [27].

In vitro coumarin-6 leakage from liposomes was measured by a dialysis method [29]. Briefly, the liposomes were placed in dialysis bag (Mw cutoff = 14,000 Da), and dialyzed against PBS at 37 °C with gentle shaking (100 rpm). At predetermined time points, aliquots were withdrawn and replenished with equal volume of PBS. The coumarin-6 content was measured by an HPLC system (Shimadzu, Japan) with an excitation wavelength of 467 nm and an emission wavelength of 502 nm [27].

2.4. Integrin αvβ3 expression in B16 and MCF-7 cells

B16 and MCF-7 cells were cultured on coverslips for 24 h at 37 °C, respectively. The cells were rinsed with PBS, fixed with 4% paraformaldehyde, blocked with 5% BSA for 1 h at room temperature and incubated with rabbit monoclonal antibodies to integrin beta 3 (ab75872, Abcam, UK). Negative controls (PBS added) were included. A Texas Red-conjugated Affinipure Goat Anti-rabbit IgG was used as secondary antibody and incubated with cells for 1 h at 37 °C. Cell nuclei were stained with Hoechst 33258, and the samples were observed using a Leica TCS SP5 confocal laser-scanning microscope (CLSM, Heidelberg, Germany).

2.5. Interaction between different RGD peptides modified liposomes and cells detected by surface plasmon resonance (SPR) technology

SPR technology was applied here to investigate the interaction of the liposomes with cells. SPR experiments were performed using a BIACORE 3000 instrument (BIACORE 3000, GE Healthcare) [30]. In brief, sensor chips (GE Healthcare, Uppsala, Sweden) were activated with 1-ethyl-3-[3-dimethylaminopropyl]carbodiimide hydrochloride (EDC) and *N*-hydroxysuccinimide (NHS). Then B16 (2×10^5 mL^{-1}) and MCF-7 (2×10^5 mL^{-1}) were covalently linked on sensor chips via the proteins on the surface of cells respectively. When the response (RU) signal reached about 300, the injection of cells was stopped followed by sensor chip blocking with acetamide. After the response (RU) signal was stable, liposomes were injected for 1 min at a 5 μL/min flow rate respectively. Before each injection, the phosphate buffer was used to wash the liposomes off the sensor chip.

2.6. Cellular uptake studies

2.6.1. Real-time confocal analysis on uptake kinetics of the nanocarriers

B16 and MCF-7 were seeded on a glass-bottom dish, respectively. The media was removed before recording images. The confocal images were recorded continuously with a Leica TCS SP2 confocal laser-scanning microscope (CLSM, Heidelberg, Germany) after the liposome solutions (containing 300 ng/mL coumarin-6) were added. This experiment was performed at 37 °C. To compare the cellular uptake of different liposomes quantitatively, regions of interest (ROI) from the whole cell were selected randomly (10 ROIs per group). The uptake kinetics was analyzed using Leica SP2 confocal software (Leica Microsystems, Heidelberg, Germany).

2.6.2. Cellular uptake mechanism studies

For observation of the distribution of the liposomes in cells, after 1 h incubation with coumarin-6-loaded liposomes (containing 300 ng/mL coumarin-6), B16 and MCF-7 were rinsed with PBS and fixed with 4% paraformaldehyde respectively. Cell nuclei were stained with Hoechst 33258, and the samples were observed using a Leica TCS SP5 confocal laser-scanning microscope (CLSM, Heidelberg, Germany).

For the receptor competition experiments, free cRGD (0.1 mg/mL) was added, and the cells were pre-incubated for 1 h prior to the addition of nanocarriers coumarin-6-loaded liposomes. Then cells were incubated with each liposome formulation (containing 300 ng/mL coumarin-6) for1 h at 37 °C. The cells were then rinsed, trypsinized, collected and lysed using RIPA solution. Methanol was used to extract the coumarin-6 that was released by the RIPA. Coumarin-6 content was measured using an HPLC system (Shimadzu, Japan) as mentioned above. The protein content was determined with a BCA assay.

2.6.3. Endocytosis pathway studies

The CCK-8 assay was applied to investigate the effect of liposomes and inhibitors on B16 cell vitality. In brief, B16 cells were seeded into 96-well plates at a density of 5000 cells per well and cultured for 24 h. The medium was then removed and the cells were cultured with free-serum RPMI-1640 containing liposomes or inhibitors. After 1 h incubation, each well was replaced with fresh free-serum RPMI-1640 and CCK-8 solution, and the cells were incubated for 1 h at 37 °C. The absorbance was determined at 450 nm using a microplate reader (Thermo Multiskan FC, America).

B16 cells were seeded into 12-well plates and incubated for 24 h at 37 °C. The media was then removed, and the cells were pre-incubated with inhibitors as illustrated in Supplemental Table S2 for 1 h. Each coumarin-6-loaded liposome formulation was added, and cells were incubated at 37 °C for 1 h. The cells were then washed, trypsinized and centrifuged. In total, 200 μL RIPA was added to lyse the cells, and methanol was used to extract the coumarin-6 that had been released in the RIPA. Coumarin-6 content was measured with an HPLC system (Shimadzu, Japan) as mentioned above. The protein content was determined with a BCA assay.

For confocal observation, after 1 h pre-incubation with inhibitors, B16 cells were incubated at 37 °C for 1 h. Then, cells were rinsed with PBS and fixed with 4% paraformaldehyde. Cell nuclei were stained with Hoechst 33258, and the samples were observed using a Leica TCS SP5 confocal laser-scanning microscope (CLSM, Heidelberg, Germany).

2.7. In vivo targeting study by near-infrared fluorescence imaging

In vivo targeting studies were performed using male C57BL/6 mice and an armpit tumor model. Approximately 5×10^6 B16 cells were implanted subcutaneously into the right flanks of the mice. When the tumor volume reached approximately 500 mm^3, the mice were randomly divided into four groups (3 mice each) and injected with 0.3 mL DiR-loaded non-targeted liposomes and three types of DiR-loaded targeted liposomes via the tail vein. The DiR dosage was 4 μg each. Anesthesia was maintained with 1.0% isoflurane in oxygen. Fluorescent images were dynamically acquired using an *in vivo* imaging system (Carestream, Fx Pro, USA) at 1, 3, 8, 12, 24 and 30 h post-injection. After 30 h, the mice were sacrificed and the tumors were excised. *Ex vivo* fluorescent images of the tumors were also detected. The mean fluorescence intensity of tumors in different groups was analyzed with the imaging station Carestream software. All of the animal experiments were performed in compliance with the Principles of Laboratory Animal Care and were approved by the Institutional Animal Care and Use Committee of Peking University.

2.8. Single-molecule imaging experiments

Fluorescence labeled RGD was obtained by conjugating Cy3 mono NHS ester (in fresh distilled DMF) to cRGD (in fresh distilled DMF) with a dye:peptide molar ratio of 1:1 according to the manufacturer's instructions. The pH was adjusted to 8.0 with triethylamine. After 120 h incubation at room temperature under moderate stirring, the resulting reaction mixture was dialyzed against deionized water for 72 h to remove unreacted dye in the dark. The final solution was lyophilized. The conjugation product (Cy3-RGD) was confirmed by MALDI–TOF MS.

A total internal reflection fluorescence microscopy (TIRFM, IX-81, Olympus) equipped with an oil-immersion objective (PlanApo × 150, NA 1.45, Olympus) was used to observe αvβ3 clustering. Specimens were illuminated with a semiconductor laser. Cy3 was excited by 561 nm. Images were acquired continuously for 10 min by charge-coupled-device (CCD) camera (Andor IXon3) after Cy3-RGD addition (0.1 ng/mL) to B16 cells. Images were analyzed using ImageJ 1.44 software.

2.9. Construction of αvβ3 clustering structural models and computation of the distance between the two RGD motifs

Based on the structure of integrin αvβ3 and the RGD binding site (PDB code: 1L5G), we constructed two extreme structural models of αvβ3 clustering. The Accelrys Discovery Studio 2.5 software package was used to analyze the distance between the two RGD binding sites in αvβ3 clustering molecular models.

The structures of diRGD and P-diRGD were calculated using a semi-empirical method with a Gaussian 09 program package. Equilibrium geometries for all of the molecules were fully optimized at the AM1 theory level. Vibrational frequencies were calculated at the same level and used to determine the nature of the stationary points.

The approximate calculation method for the distance of two neighboring RGD on the surface of moRGD-LP was as follows: The superficial area per liposome was approximate composed of N small circles with one RGD in each center. The number of small circles in moRGD-LP of radius R (in nm) was calculated using the formula $N = \rho\ (4\pi R^2/S_P)$, where ρ is the RGD density (1%) and S_P is the approximate cross-sectional area of each phospholipid (0.48 nm^2) [31]. The area per small circle $S_N = 4\pi R^2/N = S_P/\rho$. Thus, the distance of the two neighboring RGD $d1 = 2R_N = 78.196$ Å, where R_N is the radius of the small sphere.

2.10. Statistical analysis

All the experiments were repeated at least three times. Data were shown as means ± standard deviation (SD). The results were analyzed by Student's t test. P values less than 0.05 were considered as statistically significant, while less than 0.01 were highly significant.

3. Results and discussion

3.1. Preparation and characterization of RGD peptides modified liposomes

In this study, three RGD peptides, moRGD, diRGD and P-diRGD, were chosen as functional ligands to modify liposomal nanocarriers, respectively. The molecular structures of three RGD ligands are shown in Fig. 1A. Compared to diRGD, P-diRGD significantly increases the distance between two RGD motifs due to the introduction of PEG spacer. First, three ligands were successfully conjugated to DSPE–PEG–NHS respectively determined by MALDI–TOF–MS (Fig. 1B) and HPLC analysis (Supplemental Fig. S1). Then, RGD-modified liposomes were all prepared with a lipid film hydration method [28]. According to RGD associated literature [32], the appropriate surface density of RGD peptides for three liposomes was all set as 1% (mole ratio). A schematic representation of P-diRGD-LP is shown in Fig. 2A. The conjugated ligands located on the particle surface. Multiple hydrophobic fluorescence markers, including coumarin-6 and DiR, were loaded into the lipid bilayer. The particle size determined by DLS and cryo-TEM of P-diRGD-LP showed the mean size of near 100 nm and spheroid morphology (Fig. 2B and C). No significant difference in particle size and surface charge for other types of RGD-modified liposomes was detected (Fig. 2 and Supplemental Table S1). This is important because the size of liposomes specially governs its biodistribution and the variation in liposome size dictates the ligand-receptor interaction [33].

Coumarin-6 as a common fluorescent marker for nanoparticle tracing was loaded in liposomes. The encapsulation efficiencies of coumarin-6 for all types of liposomes were >80%, suggesting that coumarin-6 was well loaded in liposomes (Supplemental Table S1). The *in vitro* leakage profile of coumarin-6 from liposomes in Fig. 2D showed that less than 1% of coumarin-6 leaked out for each type of liposomes within 24 h. The incubation time of liposomes in following cellular uptake experiments was not more than 3 h, at which point the cumulative leakage was even lower than 0.5%. So, it could be predicted that most of coumarin-6 was taken up into cells in the form of liposomes.

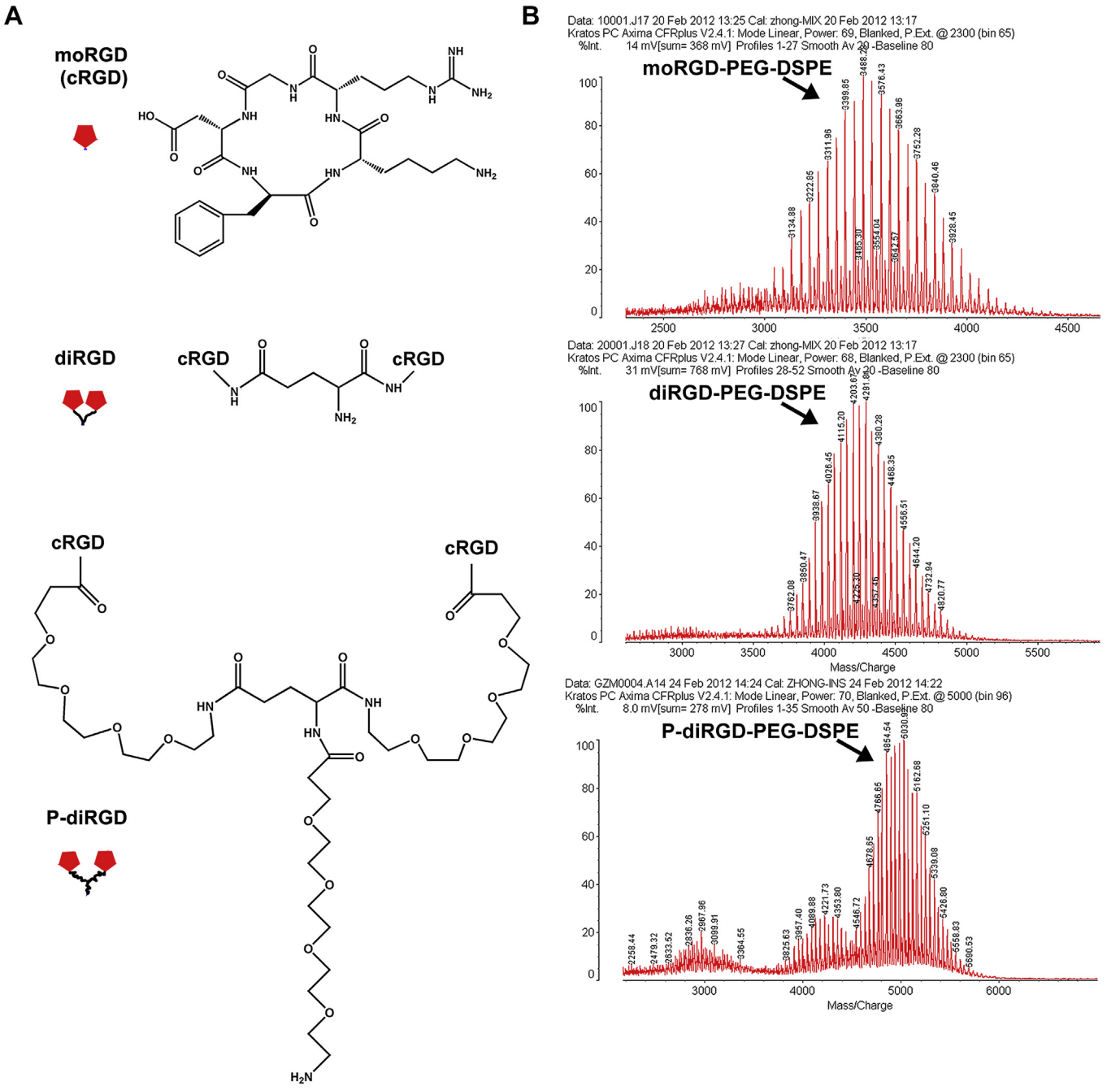

Fig. 1. (A) Chemdraw structures of moRGD (cRGD), diRGD and P-diRGD. (B) MALDI–TOF–MS analysis of moRGD–PEG–DSPE, diRGD–PEG–DSPE and P-diRGD–PEG–DSPE.

3.2. Receptor expression

Determined by immunofluorescence method, B16 cells highly expressed integrin αvβ3, while MCF-7 cells exhibited little αvβ3 expression (Supplemental Fig. S2).

3.3. Studies on the enhanced interaction of P-diRGD-LP with B16 cells

The whole uptake of nanocarriers by cells is always divided into two processes, surface binding on cell membrane and the following internalization. Firstly, to investigate the effect of RGD modification on the interaction of liposomes with cells, surface plasmon resonance (SPR), a promising technology to detect the molecular interaction in real-time by monitoring the refractive index change between the sensor surface and samples [34], was utilized here. As exhibited in Fig. 3A, B16 and MCF-7 cells, with different degrees of αvβ3 expression, were respectively immobilized on the sensor surface via covalent binding. With the subsequent flow of phosphate buffer containing different liposomes, the response (RU) signals that reflected the interaction between liposomes and cells were recorded. In terms of immobilized B16 cells, the addition of P-diRGD-LP triggered the highest response (Fig. 3B), indicating the strongest binding. However, for MCF-7 cells with little expression of αvβ3, P-diRGD-LP did not cause significant difference compared with other types of liposomes (Fig. 3C). Therefore, via SPR technology, we demonstrated that P-diRGD-LP enhanced the interaction between nanocarriers and αvβ3 highly expressed tumor cells.

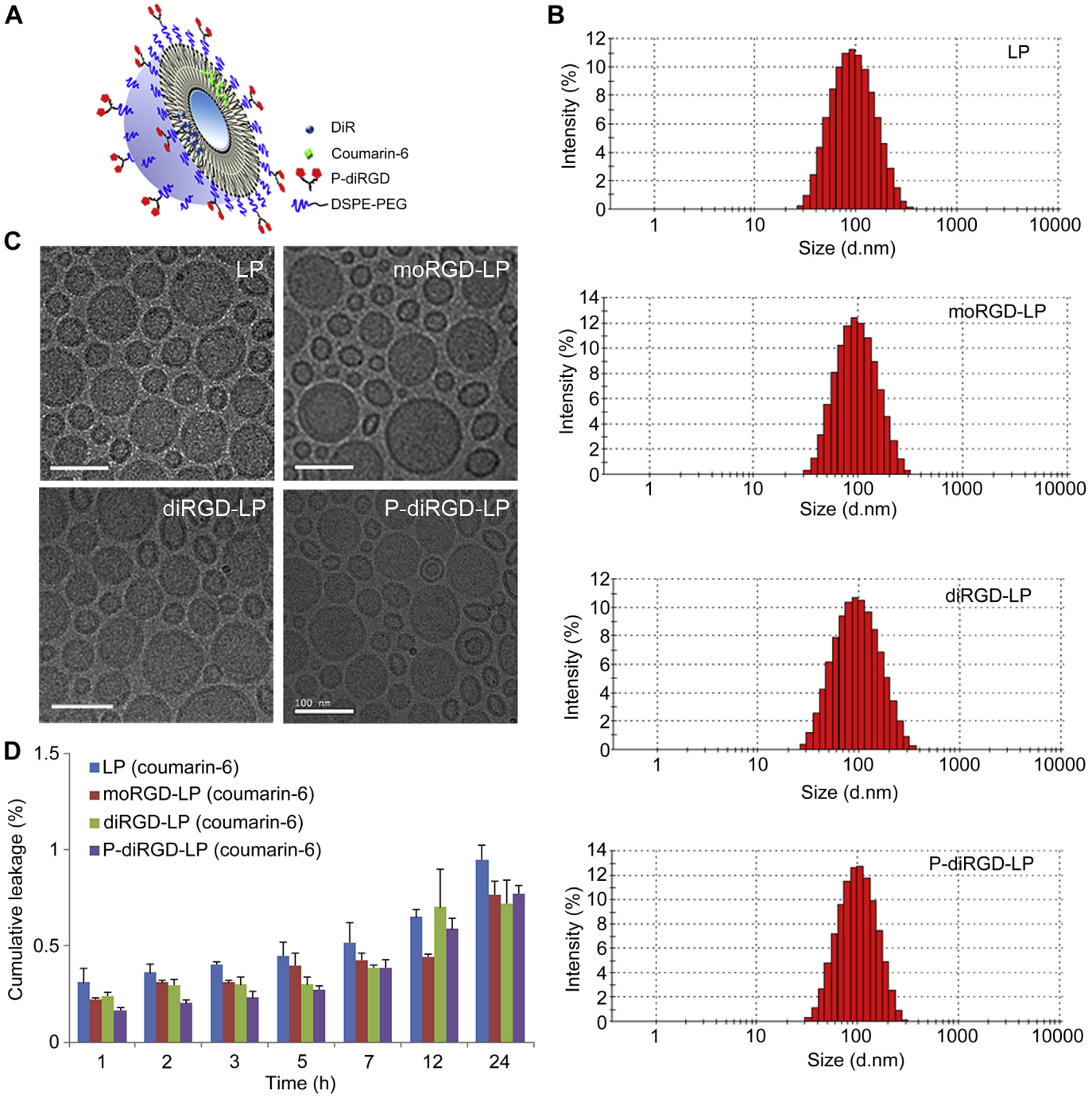

Fig. 2. (A) Schematic illustration of P-diRGD-modified liposomes loaded with DiR or coumarin-6 (P-diRGD-LP). (B) Representative particle size distribution profiles of LP, moRGD-LP, diRGD-LP and P-diRGD-LP by dynamic light scattering. (C) Typical cryogenic transmission electron microscopy (cryo-TEM) images of LP, moRGD-LP, diRGD-LP and P-diRGD-LP. Scale bar = 100 nm. (D) *In vitro* leakage profile of coumarin-6 from the liposomes in PBS. Data represented as mean ± SD ($n = 3$).

3.4. Improved cellular uptake studies of P-diRGD-LP

3.4.1. Real-time analysis on the uptake kinetics of P-diRGD-LP

Via the real-time detection by confocal laser-scanning microscope (RT-CLSM), we compared the uptake kinetics of different liposomes in B16 cell line. As exhibited in Fig. 4A, P-diRGD-LP showed faster uptake than moRGD-LP or negative control (20 s for P-diRGD-LP versus 300 s for moRGD-LP and 600 s for LP), and more cellular uptake than diRGD-LP with extension of time. Quantitative analysis (Fig. 4B) also demonstrated the similar result. So it was indicated that P-diRGD-LP had a greater targeting efficacy to αvβ3 highly expressed B16 cells compared to diRGD-LP and moRGD-LP. Additionally, the same investigation was also conducted on MCF-7 cells with negative αvβ3 expression. All liposomes exhibited very low cellular uptake during 10 min incubation (Supplemental Fig. S3). More importantly, no significant difference of uptake velocity was detected on three RGD-modified liposomes. By comparing the response of different liposomes to cellular uptake in two types of cells, we demonstrated that the modification of P-diRGD displayed better specificity to integrin αvβ3. Given the

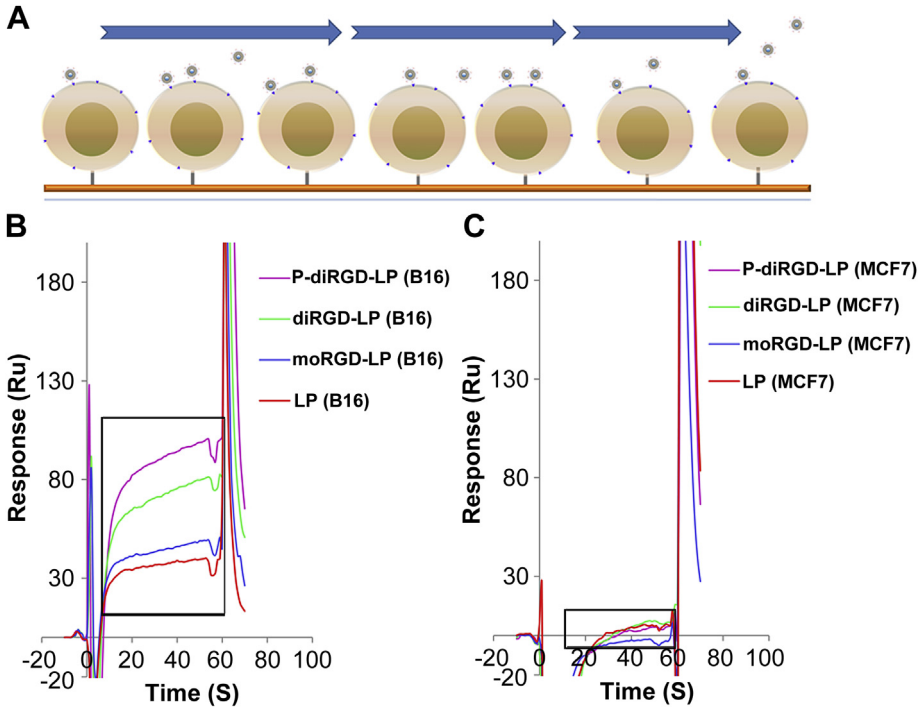

Fig. 3. SPR studies of liposome–cell interactions. (A) Schematic illustration of a sensor chip linked with cells under flowing buffer containing liposomes. (B) SPR response of different RGD peptides modified liposomes with B16 cells during a 1-min injection. (C) SPR response of different RGD peptides modified liposomes with MCF7 cells during a 1-min injection. Square frames indicate the area of response (RU).

chemical structure discrepancy of three ligands, we speculated the interval between two RGD motifs in P-diRGD might be more adaptable to the distribution of αvβ3 in cell membrane.

3.4.2. Cellular uptake mechanism studies

The distribution characteristics of P-diRGD-LP was analyzed and compared with other liposomes after 1 h incubation with B16 cells. As shown in Fig. 5A, P-diRGD-LP displayed the maximum internalization. Moreover, compared to moRGD-LP and diRGD-LP, more pronounced fluorescence was observed on cell surface in P-diRGD-LP group (red arrow heads, Fig. 5A), indicating the enhanced affinity of P-diRGD-LP with cells. For MCF-7 cells with little αvβ3 expression, no difference was found among four types of liposomes in confocal microscope images (Supplemental Fig. S4). To verify that the increased cellular uptake of P-diRGD-LP was attributed to ligand-receptor interaction but not non-specific adhesion, we performed competitive uptake investigation in B16 cells. Fig. 5B showed the significant decrease of cellular uptake of RGD-modified liposomes after the pre-incubation of free RGD. Thus it was indicated that the enhanced uptake of targeted liposomes by B16 cells was mediated by specific RGD-αvβ3 interplay.

3.4.3. Endocytosis pathway studies

We also investigated the effect of P-diRGD modification on endocytosis of liposomes. The inhibitors of different pathways are listed in Supplementary Data (Supplemental Table S2). No cytotoxicity was detected for all chosen inhibitors, confirming the feasibility of inhibition analysis (Supplemental Fig. S5). As shown in

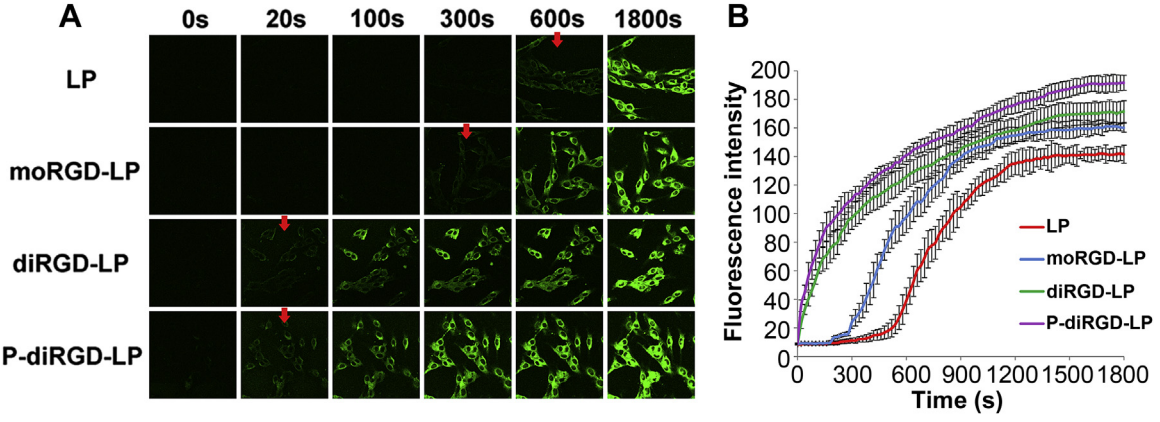

Fig. 4. Cellular uptake kinetics of different liposomes in B16 cells. (A) Real-time confocal analysis on cellular uptake of LP, moRGD-LP, diRGD-LP and P-diRGD-LP at 37 °C. Green represents coumarin-6 fluorescence. Red arrows indicate the beginning time of cellular uptake of liposomes. (B) Quantitative analysis of confocal images. Each point on the plot represents the mean fluorescence intensity obtained from 10 randomly selected ROIs ± SD (For interpretation of the references to color in this figure legend, the reader is referred to the web version of this article.).

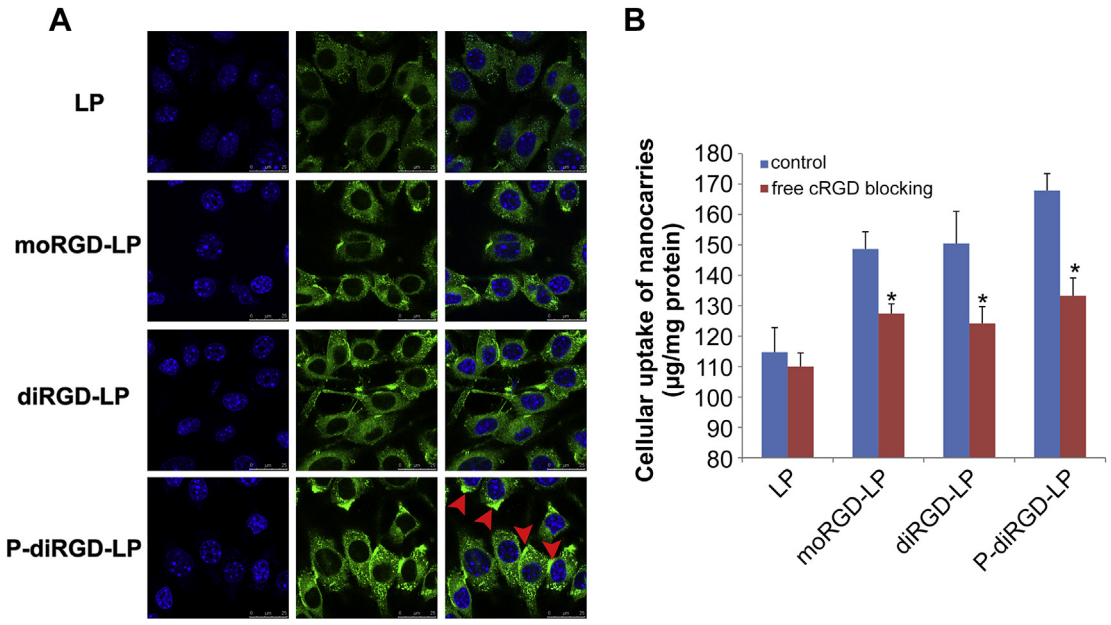

Fig. 5. (A) Confocal laser-scanning microscopy (CLSM) images of B16 cells incubated with LP, moRGD-LP, diRGD-LP and P-diRGD-LP at 37 °C for 1 h. Red arrow heads indicate the adhesion of liposomes on the cell surface. (B) Receptor competition experiments conducted in B16 cells using free cRGD blocking for 1 h prior to incubation with LP, moRGD-LP, diRGD-LP or P-diRGD-LP at 37 °C * indicate $p < 0.05$ versus their respective control (For interpretation of the references to color in this figure legend, the reader is referred to the web version of this article.).

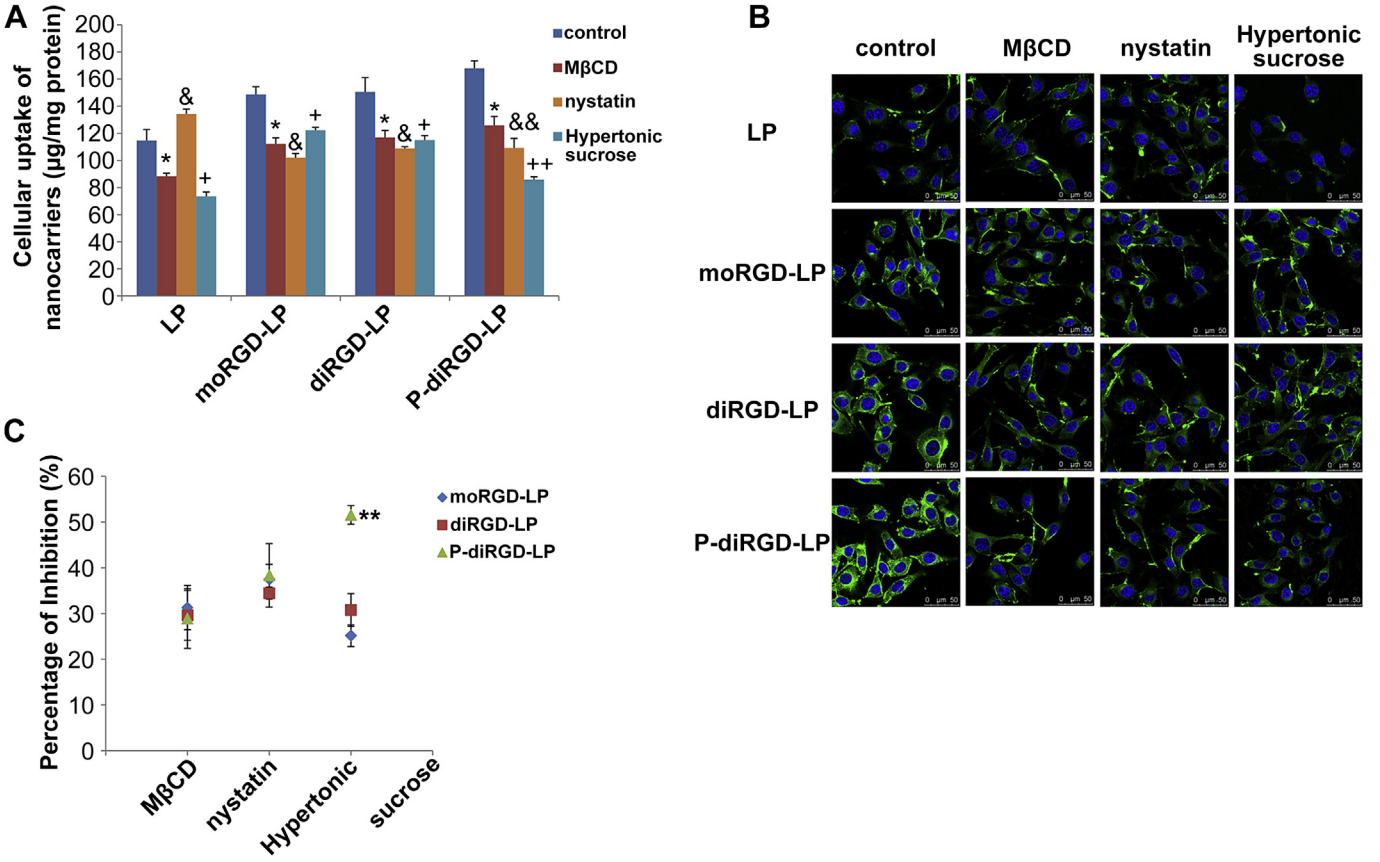

Fig. 6. (A) Effects of inhibitors on cellular uptake of LP, moRGD-LP, diRGD-LP or P-diRGD-LP in B16 cells. Cells were pre-incubated with the inhibitors for 1 h at 37 °C. Groups treated with LP, moRGD-LP, diRGD-LP or P-diRGD-LP only were used as controls. *, +, and & indicate $p < 0.05$ versus their respective control. && and ++ indicate $p < 0.01$ versus their respective control. (B) Confocal laser-scanning microscopy (CLSM) images of B16 cells incubated with LP, moRGD-LP, diRGD-LP or P-diRGD-LP at 37 °C for 1 h after pre-incubation with the inhibitors. (C) Comparison of inhibitors on the uptake inhibition of moRGD-LP, diRGD-LP and P-diRGD-LP. ** indicates $p < 0.01$ versus moRGD-LP and diRGD-LP groups.

Fig. 6A, MβCD and nystatin, the inhibitors of caveolae-dependent endocytosis [35], and hypertonic sucrose as the inhibitor of clathrin-mediated endocytosis [36], all significantly decreased the cellular uptake of three types of RGD-modified liposomes. This result indicated that both caveolae-dependent endocytosis and clathrin-mediated endocytosis were involved in αvβ3-mediated endocytosis. As for the increased cellular uptake of LP for nystatin, it was suggested that other endocytosis pathways might be activated or upregulated in the presence of this inhibitor [35]. The confocal microscope images further demonstrated the same endocytosis result (Fig. 6B). Notably, by calculating the percentage of inhibition, hypertonic sucrose showed greater effect for the endocytosis of P-diRGD-LP compared to moRGD-LP and diRGD-LP (51% for P-diRGD-LP versus 30% for diRGD-LP and 25% for moRGD-LP, Fig. 6C). However, the inhibition effect of caveolae-dependent endocytosis inhibitors on the uptake of three types of liposomes was not significantly different. Thus it revealed that, other than the modification of moRGD and diRGD, flexible P-diRGD significantly increased the cellular uptake of liposomes via clathrin-mediated pathway. Recently it was reported that a multimeric RGD peptide increased αvβ3 internalization via clathrin-dependent route [37]. So we deemed that the improved endocytosis of P-diRGD-LP was triggered by the interaction of bivalent P-diRGD with αvβ3.

3.5. Enhanced in vivo targeting efficacy studies of P-diRGD-LP

To further evaluate the targeting efficacy of P-diRGD-LP *in vivo*, we performed near-infrared fluorescence (NIRF) imaging in B16 melanoma bearing mice. As shown in Fig. 7A, all three types of RGD-modified liposomes exhibited much stronger signals in tumor than non-targeted group (LP) during the whole experiment. Strikingly, more pronounced fluorescence accumulation in the tumor region was observed in P-diRGD-LP group at each time point compared with moRGD-LP and diRGD-LP. *Ex vivo* images of dissected tumors also indicated the higher fluorescence accumulation in tumor tissue for P-diRGD-LP administration (Fig. 7B). Besides, the semiquantified data showed the highest fluorescence intensity in tumor area in P-diRGD-LP group (Fig. 7C), about 2.4-fold that of moRGD-LP and 2.8-fold that of diRGD-LP at 3 h. Therefore, *in vivo* assay confirmed that the modification of P-diRGD could enhance the targeting efficacy of liposomes for αvβ3 highly expressing tumors.

3.6. Mechanism analysis on improved targeting efficacy of P-diRGD-LP

3.6.1. Validation of integrin αvβ3 clustering activated by RGD binding

Given the discrepancy of targeting efficacy between P-diRGD-LP and other RGD-LP, we hypothesized that P-diRGD-LP might be better adapt to the receptor change during the interplay of RGD with αvβ3.

To validate the phenomenon of αvβ3 clustering in cell membrane of living B16 cells, we conducted single-molecule imaging studies using a total internal reflection fluorescence microscope (TIRFM, IX-81, Olympus). Cy3-labeled RGD (Cy3-RGD) was synthesized by a reaction between Cy3-NHS and cyclic RGD (Supplemental Fig. S6). By setting the focal plane of TIRFM at plasma membrane, tremendous fluorescent spots quickly appeared after the addition of Cy3-RGD as shown in Fig. 8A, directly confirming the interaction of RGD with membrane αvβ3. We further traced the movement of fluorescent spots on cell membrane. As shown in Fig. 8B, two fluorescent spots moved laterally towards

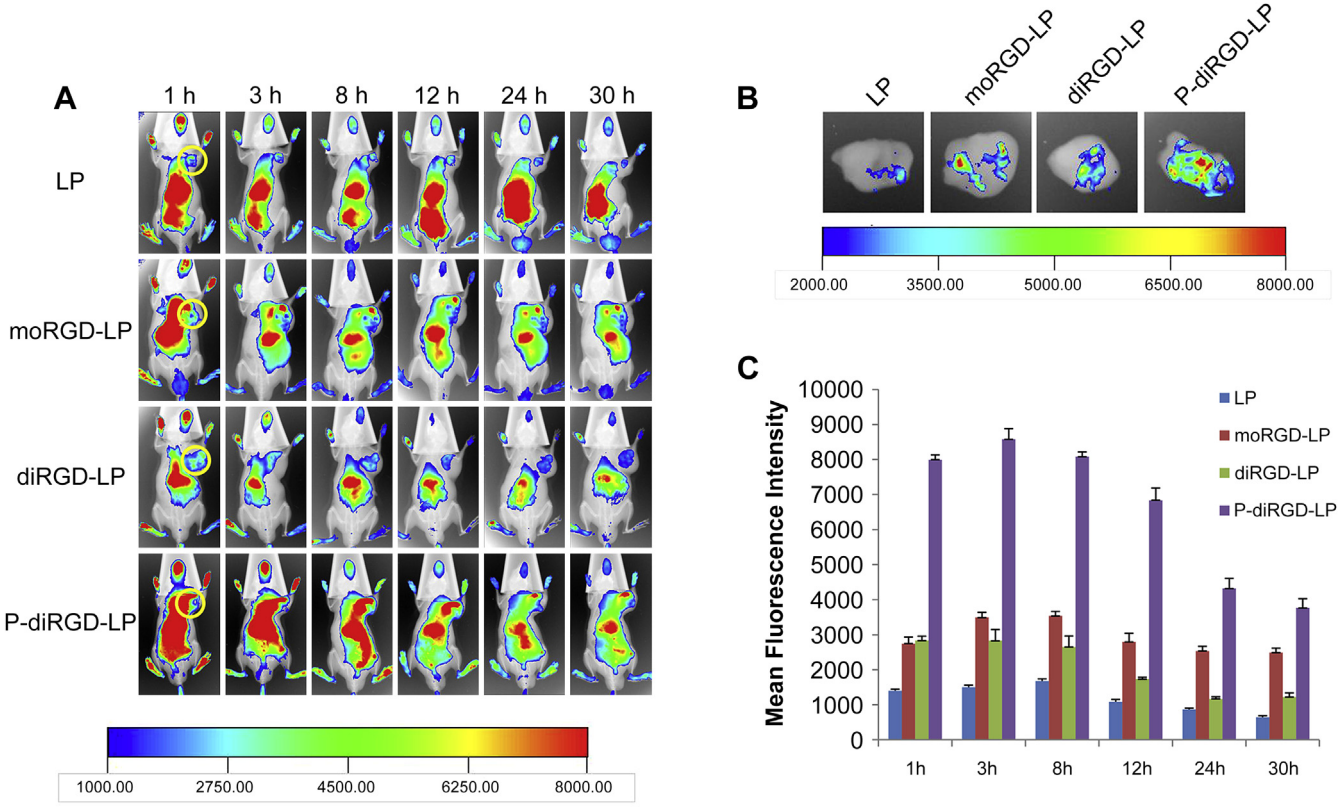

Fig. 7. Evaluation of tumor targeting using DiR-loaded liposomes *in vivo* in B16-tumor bearing male C57BL/6 mice. (A) *In vivo* fluorescent images of mice treated with LP, moRGD-LP, diRGD-LP or P-diRGD-LP at predetermined time points after administration. Yellow circles indicate the tumor region. (B) *Ex vivo* fluorescent images of tumors 30 h after DiR treatment. (C) Semiquantified data of the fluorescence intensity in tumor area at different time points after administration with LP, moRGD-LP, diRGD-LP or P-diRGD-LP. Data represent means ± SD ($n = 3$) (For interpretation of the references to color in this figure legend, the reader is referred to the web version of this article.).

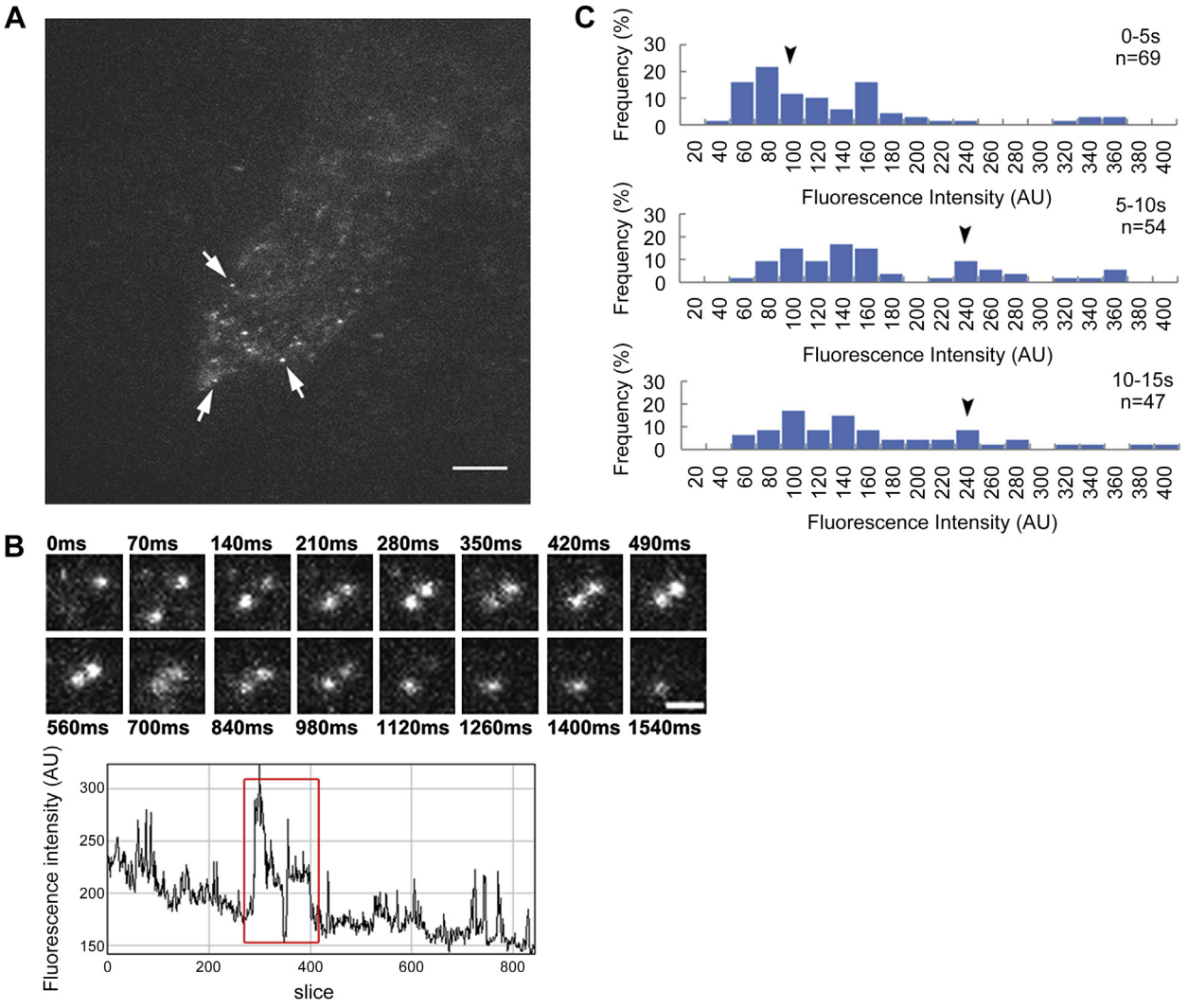

Fig. 8. Demonstration of αvβ3 clustering on the surface of living B16 cells. (A) The image of living B16 cells acquired immediately after Cy3-RGD addition (0.1 ng/mL) using a TIRFM. The scale bar represents 5 μm. White arrows indicate fluorescent spots of Cy3-RGD binding with membrane αvβ3. (B) Movement of two fluorescent spots on the cell surface (upper panel) and the dynamic variation of fluorescence intensity (lower panel). The scale bar represents 1 μm. The square frame indicates a two-step gradient photobleaching process of the spot in the image above. (C) Fluorescence intensity distribution of Cy3-RGD spots within 0–5 s, 5–10 s and 10–15 s. Black arrow heads indicate the appearance of spots with higher intensity(For interpretation of the references to color in this figure legend, the reader is referred to the web version of this article.).

each other, collided and finally photobleached (Fig. 8B, upper panel). The dynamic variation of the fluorescence intensity also exhibited the instantaneous increase and a two-step gradient photobleaching process (Fig. 8B, lower panel). These observations demonstrated the dimerization of αvβ3 triggered by RGD binding. Besides, the statistical analysis on the intensity distribution of about 50 fluorescent spots at different periods in Fig. 8C showed the appearance of more spots with stronger intensity with time (black arrows), further suggesting that αvβ3 in cell membrane were activated by RGD motif and formed clusters. It is reported that receptor activation is a feedback of ligand binding [8,38], and the receptor dimerization may further initiate its clustering [39]. Thus we demonstrated that the RGD–αvβ3 interaction was not a simple bond, but a dynamic process accompanied by receptor clustering.

3.6.2. *Matched distance between the two RGD motifs for simultaneous binding of two integrin αvβ3 molecules*

Currently, little is known on the precise conformation characteristics of αvβ3 clustering. After the activation by RGD ligands, αvβ3 might assemble from every direction, causing the variability of intervals among RGD binding sites in clusters. So, based on the chemical structure of integrin αvβ3 (PDB code: 1L5G) and the computational chemistry analysis on the RGD binding site of αvβ3 [17], we constructed two extreme structural models for αvβ3 dimerization in clusters [40]. As shown in Fig. 9A, the ββ model had the minimum distance (41.916 Å) between the two RGD binding sites (green color, Fig. 9A), and the αα model provided the maximum length (65.779 Å). This result indicated that the appropriate interval between RGD motifs for simultaneous binding with two molecules of αvβ3 ranged between 41.916 Å and 65.779 Å. Generally, the structure model of integrin αvβ3 (PDB code: 1L5G) is low in activity with static configuration, while actual integrin αvβ3 is high in activity with upright configuration. The speculation based on static structure instead of active structure may bring some deviation. However, by construction of the two extreme structural models for αvβ3 dimerization in clusters, we provide the theoretical range of the distance of adjacent binding sites, which helps to analyze the mechanism of improved targeting efficacy of P-diRGD-LP.

Then, we compared this result with the distance between the RGD motifs of different RGD-modified liposomes. Relied on the density of moRGD-modified on the liposomes and the cross-sectional area of phospholipid molecule [31], the dynamic mean distance between

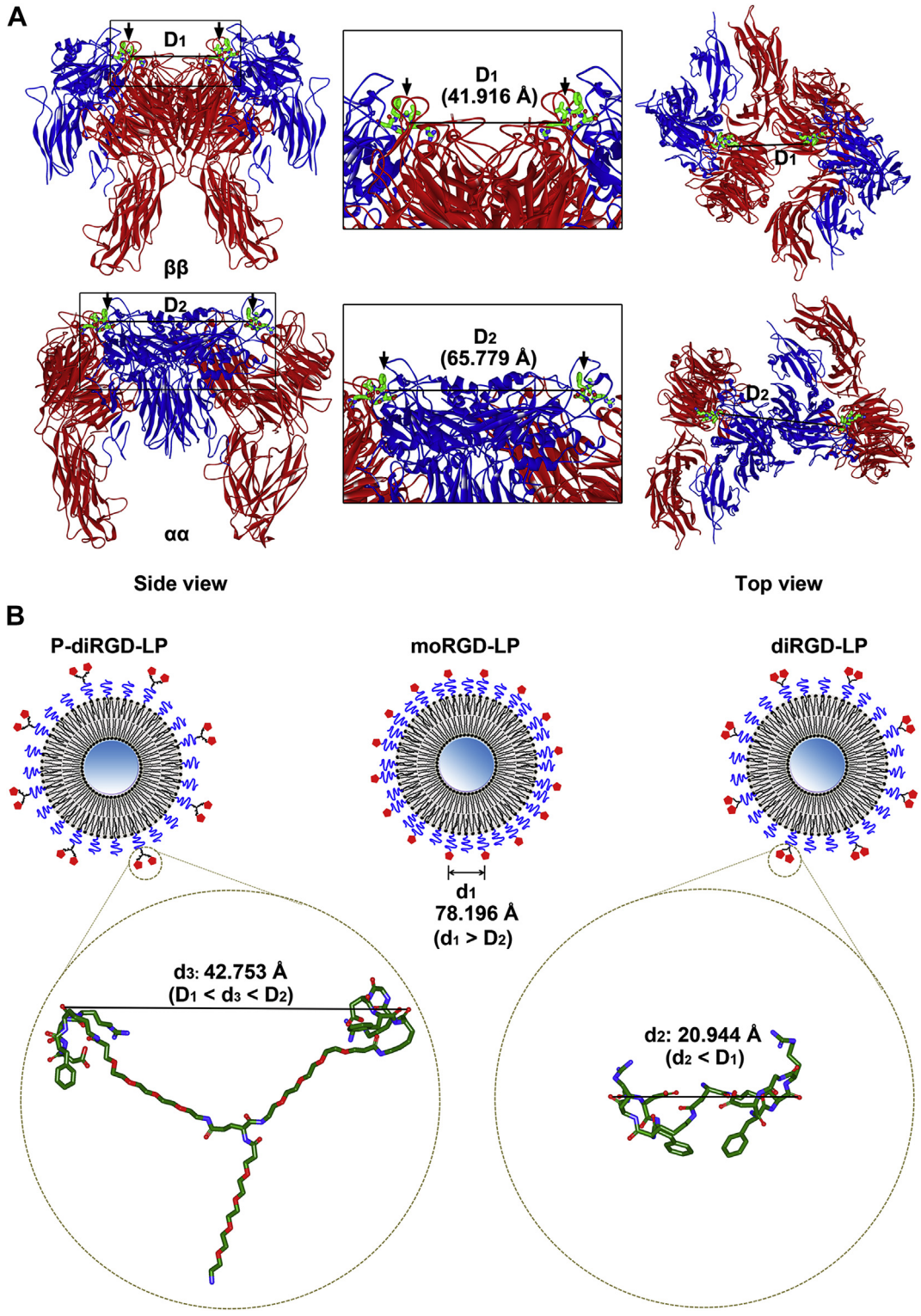

Fig. 9. Construction of 3D models of αvβ3 clustering and calculation of the distance between two RGD motifs. (A) Two 3D models of αvβ3 clustering. The RGD binding site distance between the two adjacent αvβ3 was calculated using the Accelrys Discovery Studio 2.5 software package. Black arrows indicate RGD binding sites. (B) Schematic representation of the RGD interval of different RGD-modified liposomes. The structures of diRGD and P-diRGD were calculated using a Gaussian 09 program package.

adjacent RGD motifs on moRGD-LP surface was calculated as 78.196 Å. Computational chemistry analysis further computed the RGD intervals of diRGD and P-diRGD to be 20.944 Å and 42.753 Å respectively. During the simulation analysis, equilibrium geometries of diRGD and P-diRGD molecules were fully optimized and the distance between the two RGD motifs was calculated based on the most stable conformation. Under the condition of the same RGD number, it was interesting to find that only the RGD interval of P-diRGD-LP matched the interval range in αvβ3 clustering (moRGD-LP: 78.196 Å; diRGD-LP: 20.944 Å; P-diRGD-LP: 42.753 Å) (Fig. 9B). It should be noted that the calculated distance of RGD motifs for different ligands was not constant because of the molecular movement. Nonetheless,

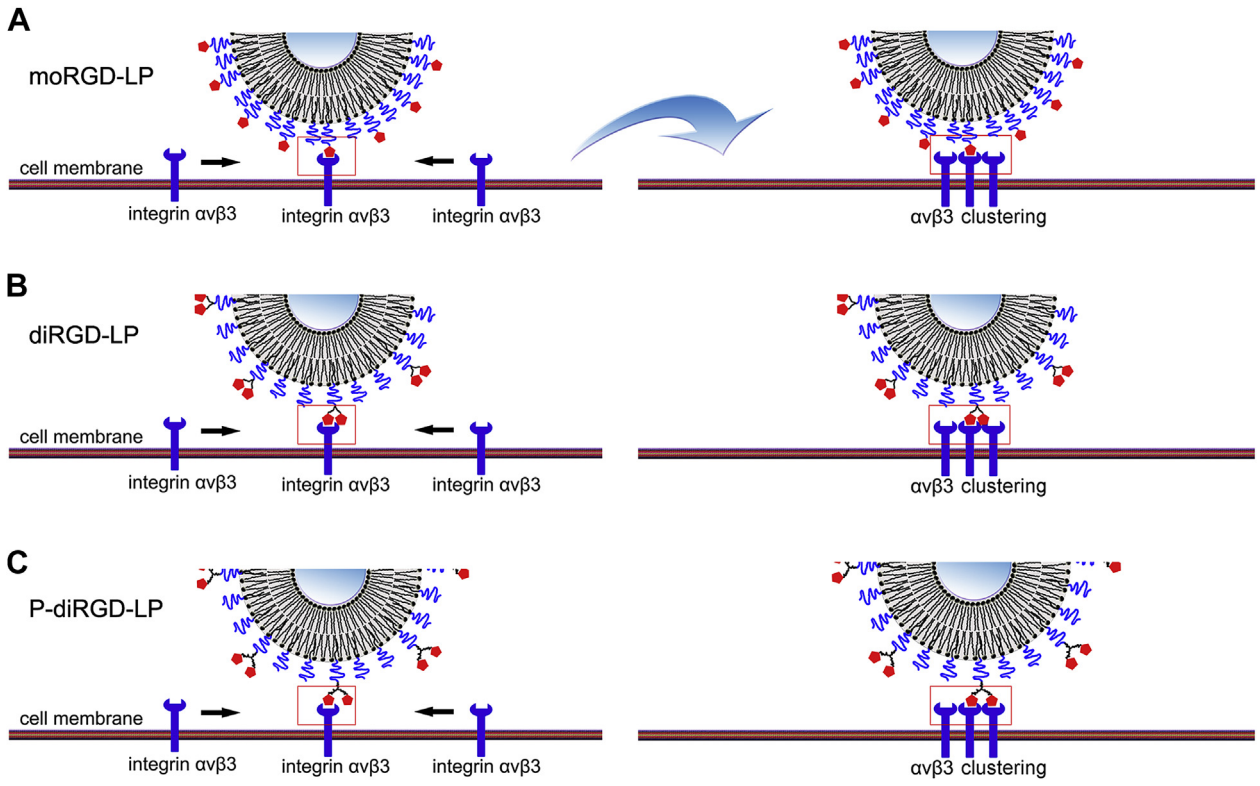

Fig. 10. Schematic illustration of the interactions between different RGD-modified nanocarriers with adjacent binding sites in αvβ3 clustering. (A) For moRGD-LP, the two RGD molecules on the surface of liposomes were too far to bind two αvβ3 molecules simultaneously. (B) For diRGD-LP, the distance between the two RGD motifs was much shorter than the distance between the two αvβ3 binding sites in the case of αvβ3 clustering. (C) The distance between the two RGD motifs of P-diRGD-LP was just compatible for simultaneous binding of two integrin αvβ3 molecules in the case of αvβ3 clustering.

the simulation result rationally provided a scientific dynamic analysis and might reflect the real conformation of RGD ligands in stable condition. So we demonstrated that P-diRGD-LP could respond to receptor change via the simultaneous binding of P-diRGD with adjacent binding sites in αvβ3 clustering. In single αvβ3 case, the interaction mechanism studies suggest a proper concentration of RGD peptides is required to achieve optimum binding [41]. The concentration of RGD is not the greater the better, and the distance among RGD should not be too close. The linker among RGD motifs promotes RGD binding to the adjacent integrin αvβ3, avoiding gather in multiple RGD system [42,43]. In the case of αvβ3 clustering, the intervals among the integrin αvβ3 changes, so the ligand interval becomes significant. Namely, the proper linker length among RGD motifs is important for the simultaneous binding of adjacent αvβ3. Neither too long nor too short interval is suitable in the case of αvβ3 clustering. Thus, the ligand interval plays a key role in the interaction between RGD peptides and clustered αvβ3. As illustrated in Fig. 10, we concluded that the distance between the two RGD motifs of P-diRGD-LP was compatible for simultaneous binding with adjacent binding sites in the case of αvβ3 clustering. For diRGD-LP, the distance between the two RGD motifs was much shorter than the interval between two binding sites. While for moRGD-LP, the two RGD molecules on the surface of liposomes were too far to bind with adjacent αvβ3 simultaneously. As a result, P-diRGD-LP enhanced the affinity of liposomes with cell membrane and improved the cellular uptake for targeting delivery.

4. Conclusion

In this study, we designed and constructed three RGD-modified nanocarriers with different ligand intervals: moRGD-LP, diRGD-LP and P-diRGD-LP. *In vitro*, P-diRGD-LP demonstrated strongest interaction with B16 cells and highest cellular uptake in B16 cells. The enhanced endocytosis of P-diRGD-LP was αvβ3-mediated and mainly via a clathrin-involved pathway. Besides, P-diRGD-LP significantly improved the targeting efficacy to αvβ3-positive tumors *in vivo*. Further, the αvβ3 clustering was validated by the single-molecule imaging study. Finally, the matching analysis by the construction of 3D models of αvβ3 clustering together with the computation of the ligand distance between adjacent RGD motifs revealed that P-diRGD-LP provided the best matching to αvβ3 clustering. Therefore, we anticipate that the design of targeted nanocarriers against receptor clustering will provide new insight into the anticancer therapy.

Acknowledgments

We thank Professor Liangyi Chen (Lab of Cell Secretion and Metabolism, Institute of Molecular Medicine, Peking University and National Center for Nanoscience and Technology, Beijing, PR China) for his generous offer of the TIRFM. This study was supported by the National Natural Science Foundation of China (No. 81130059 and 81273456), the National Basic Research Program of China (No. 2009CB930300) and Innovation Team of Ministry of Education (No. BMU20110263).

Appendix A. Supplementary data

Supplementary data related to this article can be found at http://dx.doi.org/10.1016/j.biomaterials.2014.04.031.

References

[1] Tam YY, Chen S, Zaifman J, Tam YK, Lin PJ, Ansell S, et al. Small molecule ligands for enhanced intracellular delivery of lipid nanoparticle formulations of siRNA. Nanomedicine 2013;9(5):665–74.

[2] Hossen MN, Kajimoto K, Akita H, Hyodo M, Ishitsuka T, Harashima H. Ligand-based targeted delivery of a peptide modified nanocarrier to endothelial cells in adipose tissue. J Control Release 2010;147(2):261–8.
[3] Zhao P, Lane TR, Gao HG, Hurst DP, Kotsikorou E, Le L, et al. Crucial positively charged residues for ligand activation of the GPR35 receptor. J Biol Chem 2014;289(6):3625–38.
[4] Ketchum C, Miller H, Song W, Upadhyaya A. Ligand mobility regulates B cell receptor clustering and signaling activation. Biophys J 2014;106(1):26–36.
[5] Cheng Z, Al Zaki A, Hui JZ, Muzykantov VR, Tsourkas A. Multifunctional nanoparticles: cost versus benefit of adding targeting and imaging capabilities. Science 2012;338(6109):903–10.
[6] Hunt KK, Vorburger SA. Tech.Sight. Gene therapy. Hurdles and hopes for cancer treatment. Science 2002;297(5580):415–6.
[7] Sako Y, Minoghchi S, Yanagida T. Single-molecule imaging of EGFR signalling on the surface of living cells. Nat Cell Biol 2000;2(3):168–72.
[8] Welf ES, Naik UP, Ogunnaike BA. A spatial model for integrin clustering as a result of feedback between integrin activation and integrin binding. Biophys J 2012;103(6):1379–89.
[9] Himanen JP, Yermekbayeva L, Janes PW, Walker JR, Xu K, Atapattu L, et al. Architecture of Eph receptor clusters. Proc Natl Acad Sci U S A 2010;107(24):10860–5.
[10] Wang Q, Dierkes R, Kaufmann R, Cremer C. Quantitative analysis of individual hepatocyte growth factor receptor clusters in influenza A virus infected human epithelial cells using localization microscopy. Biochim Biophys Acta 2014;1838(4):1191–8.
[11] Caré BR, Soula HA. Impact of receptor clustering on ligand binding. BMC Syst Biol 2011;5:48.
[12] McQuade P, KnIght LC. Radiopharmaceuticals for targeting the angiogenesis marker alpha(v)beta(3). Q J Nucl Med 2003;47(3):209–20.
[13] Chen X, Sievers E, Hou Y, Park R, Tohme M, Bart R, et al. Integrin alpha v beta 3-targeted imaging of lung cancer. Neoplasia 2005;7(3):271–9.
[14] Seftor RE, Seftor EA, Gehlsen KR, Stetler-Stevenson WG, Brown PD, Ruoslahti E, et al. Role of the alpha v beta 3 integrin in human melanoma cell invasion. Proc Natl Acad Sci U S A 1992;89(5):1557–61.
[15] Gladson CL, Cheresh DA. Glioblastoma expression of vitronectin and the alpha v beta 3 integrin. Adhesion mechanism for transformed glial cells. J Clin Invest 1991;88(6):1924–32.
[16] Xiong JP, Stehle T, Diefenbach B, Zhang R, Dunker R, Scott DL, et al. Crystal structure of the extracellular segment of integrin alpha Vbeta3. Science 2001;294(5541):339–45.
[17] Xiong JP, Stehle T, Zhang R, Joachimiak A, Frech M, Goodman SL, et al. Crystal structure of the extracellular segment of integrin alpha Vbeta3 in complex with an Arg–Gly–Asp ligand. Science 2002;296(5565):151–5.
[18] Ruoslahti E. RGD and other recognition sequences for integrins. Annu Rev Cell Dev Biol 1996;12:697–715.
[19] Dijkgraaf I, Beer AJ, Wester HJ. Application of RGD-containing peptides as imaging probes for alphavbeta3 expression. Front Biosci (Landmark Ed) 2009;14:887–99.
[20] Beer AJ, Schwaiger M. Imaging of integrin alphavbeta3 expression. Cancer Metastasis Rev 2008;27(4):631–44.
[21] Pike DB, Ghandehari H. HPMA copolymer-cyclic RGD conjugates for tumor targeting. Adv Drug Deliv Rev 2010;62(2):167–83.
[22] Ruoslahti E, Bhatia SN, Sailor MJ. Targeting of drugs and nanoparticles to tumors. J Cell Biol 2010;188(6):759–68.
[23] Chen K, Chen X. Integrin targeted delivery of chemotherapeutics. Theranostics 2011;1:189–200.
[24] Liu S. Radiolabeled cyclic RGD peptides as integrin alpha(v)beta(3)-targeted radiotracers: maximizing binding affinity via bivalency. Bioconjug Chem 2009;20(12):2199–213.
[25] Liu Z, Shi J, Jia B, Yu Z, Liu Y, Zhao H, et al. Two ^{90}Y-labeled multimeric RGD peptides RGD4 and 3PRGD2 for integrin targeted radionuclide therapy. Mol Pharmacol 2011;8(2):591–9.
[26] Shi J, Kim YS, Zhai S, Liu Z, Chen X, Liu S. Improving tumor uptake and pharmacokinetics of (64)Cu-labeled cyclic RGD peptide dimers with Gly(3) and PEG(4) linkers. Bioconjug Chem 2009;20(4):750–9.
[27] Du W, Fan Y, Zheng N, He B, Yuan L, Zhang H, et al. Transferrin receptor specific nanocarriers conjugated with functional 7peptide for oral drug delivery. Biomaterials 2013;34(3):794–806.
[28] Wang Z, Yu Y, Dai W, Cui J, Wu H, Yuan L, et al. A specific peptide ligand-modified lipid nanoparticle carrier for the inhibition of tumor metastasis growth. Biomaterials 2013;34(3):756–64.
[29] Zhang Y, Zhang H, Wang X, Wang J, Zhang X, Zhang Q. The eradication of breast cancer and cancer stem cells using octreotide modified paclitaxel active targeting micelles and salinomycin passive targeting micelles. Biomaterials 2012;33(2):679–91.
[30] Quinn JG, O'Neill S, Doyle A, McAtamney C, Diamond D, MacCraith BD, et al. Development and application of surface plasmon resonance-based biosensors for the detection of cell-ligand interactions. Anal Biochem 2000;281(2):135–43.
[31] Suga K, Umakoshi H. Detection of nanosized ordered domains in DOPC/DPPC and DOPC/Ch binary lipid mixture systems of large unilamellar vesicles using a TEMPO quenching method. Langmuir 2013;29(15):4830–8.
[32] Chen CW, Lu DW, Yeh MK, Shiau CY, Chiang CH. Novel RGD-lipid conjugate-modified liposomes for enhancing siRNA delivery in human retinal pigment epithelial cells. Int J Nanomedicine 2011;6:2567–80.
[33] Kibria G, Hatakeyama H, Ohga N, Hida K, Harashima H. The effect of liposomal size on the targeted delivery of doxorubicin to Integrin αvβ3-expressing tumor endothelial cells. Biomaterials 2013;34(22):5617–27.
[34] Peiris D, Markiv A, Curley GP, Dwek MV. A novel approach to determining the affinity of protein-carbohydrate interactions employing adherent cancer cells grown on a biosensor surface. Biosens Bioelectron 2012;35(1):160–6.
[35] Chen Y, Wang S, Lu X, Zhang H, Fu Y, Luo Y. Cholesterol sequestration by nystatin enhances the uptake and activity of endostatin in endothelium via regulating distinct endocytic pathways. Blood 2011;117(23):6392–403.
[36] McMahon HT, Boucrot E. Molecular mechanism and physiological functions of clathrin-mediated endocytosis. Nat Rev Mol Cell Biol 2011;12(8):517–33.
[37] Sancey L, Garanger E, Foillard S, Schoehn G, Hurbin A, Albiges-Rizo C, et al. Clustering and internalization of integrin alphavbeta3 with a tetrameric RGD-synthetic peptide. Mol Ther 2009;17(5):837–43.
[38] Cluzel C, Saltel F, Lussi J, Paulhe F, Imhof BA, Wehrle-Haller B. The mechanisms and dynamics of (alpha)v(beta)3 integrin clustering in living cells. J Cell Biol 2005;171(2):383–92.
[39] Brinkerhoff CJ, Linderman JJ. Integrin dimerization and ligand organization: key components in integrin clustering for cell adhesion. Tissue Eng 2005;11(5–6):865–76.
[40] Gottschalk KE, Kessler H. A computational model of transmembrane integrin clustering. Structure 2004;12(6):1109–16.
[41] Yu YP, Wang Q, Liu YC, Xie Y. Molecular basis for the targeted binding of RGD-containing peptide to integrin αVβ3. Biomaterials 2014;35(5):1667–75.
[42] Wu Y, Zhang XZ, Xiong ZM, Cheng Z, Fisher DR, Liu S, et al. MicroPET imaging of glioma integrin αvβ3 expression using ^{64}Cu-labeled tetrameric RGD peptide. J Nucl Med 2005;46(10):1707–18.
[43] Liu S. Radiolabeled multimeric cyclic RGD peptides as integrin alphavbeta3 targeted radiotracers for tumor imaging. Mol Pharmacol 2006;3(5):472–87.